



Article

BN-PVDF/rGO-PVDF Laminate Nanocomposites for Energy Storage Applications

Okikiola Ganiu Agbabiaka ^{1,*} , Miracle Hope Adegun ¹, Kit-Ying Chan ², Heng Zhang ¹, Xi Shen ^{1,2} and Jang-Kyo Kim ^{1,3}

- ¹ Department of Mechanical and Aerospace Engineering, Hong Kong University of Science and Technology, Hong Kong, China
² Department of Aeronautical and Aviation Engineering, Hong Kong Polytechnic University, Hong Kong, China
³ School of Mechanical and Manufacturing Engineering, University of New South Wales, Sydney, NSW 2052, Australia
* Correspondence: ogagbabiaka@connect.ust.hk; Tel.: +852-56250848

Abstract: The increasing demand for high energy storage devices calls for concurrently enhanced dielectric constants and reduced dielectric losses of polymer dielectrics. In this work, we rationally design dielectric composites comprising aligned 2D nanofillers of reduced graphene oxide (rGO) and boron nitride nanosheets (BNNS) in a polyvinylidene fluoride (PVDF) matrix through a novel press-and-fold technique. Both nanofillers play different yet complementary roles: while rGO is designed to enhance the dielectric constant through charge accumulation at the interfaces with polymer, BNNS suppress the dielectric loss by preventing the mobility of free electrons. The microlaminate containing eight layers each of rGO/PVDF and BNNS/PVDF films exhibits remarkable dielectric performance with a dielectric constant of 147 and an ultralow dielectric loss of 0.075, due to the synergistic effect arising from the alternately electrically conductive and insulating films. Consequently, a maximum energy density of 3.5 J/cm^3 —about 18 times the bilayer composite counterpart—is realized. The high thermal conductivities of both nanofillers and their alignment endow the microlaminate with an excellent in-plane thermal conductivity of $6.53 \text{ Wm}^{-1}\text{K}^{-1}$, potentially useful for multifunctional applications. This work offers a simple but effective approach to fabricating a composite for high dielectric energy storage using two different 2D nanofillers.

Keywords: boron nitride nanosheets (BNNS); reduced graphene oxides (rGO); multiple layer structure; dielectric composites; charge energy density



Citation: Agbabiaka, O.G.; Adegun, M.H.; Chan, K.-Y.; Zhang, H.; Shen, X.; Kim, J.-K. BN-PVDF/rGO-PVDF Laminate Nanocomposites for Energy Storage Applications. *Nanomaterials* **2022**, *12*, 4492. <https://doi.org/10.3390/nano12244492>

Academic Editor: Carlos Miguel Costa

Received: 19 November 2022

Accepted: 12 December 2022

Published: 19 December 2022

Publisher's Note: MDPI stays neutral with regard to jurisdictional claims in published maps and institutional affiliations.



Copyright: © 2022 by the authors. Licensee MDPI, Basel, Switzerland. This article is an open access article distributed under the terms and conditions of the Creative Commons Attribution (CC BY) license (<https://creativecommons.org/licenses/by/4.0/>).

1. Introduction

The growing interest in electrical energy storage devices requires rational design of polymer-based composites with concomitantly high dielectric constants (k) and low dielectric losses ($\tan \delta$) [1–7]. Polymer dielectrics have received much attention because of their light weight, low cost, ease of processing, high breakdown strength (E_b), and higher flexibility than ceramic and metallic counterparts, making them suitable for emerging applications, such as wearable electronics, flexible energy storage devices, and hybrid vehicles [6]. Examples of polymers used for dielectrics include polyvinylidene fluoride (PVDF) [8], epoxy [9], polyimide (PI) [1], polyurethane (PU) [10], poly(ethylene terephthalate) (PET) [11], poly(methyl methacrylate) (PMMA) [12], and biaxially oriented polypropylene (BOPP) [13]. However, their low dielectric constants—usually below 10—greatly limit their practical applications [14].

Many attempts have been directed towards enhancing the k of polymer dielectrics, especially by incorporating high k ceramic fillers such as lead zirconate titanate ($\text{Pb}[\text{Zr}_x\text{Ti}_{1-x}]\text{O}_3$ ($0 \leq x \leq 1$) [15], calcium copper titanate ($\text{CaCu}_3\text{Ti}_4\text{O}_{12}$) [3], and barium titanate (BaTiO_3) [16], into the polymer matrix. However, the improved k often comes at the expense of higher $\tan \delta$ due to energy dissipation and high-field hysteresis losses. The

mechanical properties of the composites also deteriorate because the high filler loading required to achieve high k tends to agglomerate and weaken the filler–matrix interfacial bond [10,17,18]. Meanwhile, the use of conductive fillers such as carbon nanotubes (CNTs) and graphene in a polymer matrix is a proven means of achieving high k ranging from 100 to 10,000 (at 1 kHz) at a low filler loading, thanks to large interfacial polarization aided by the wide contrast in electrical conductivity (EC) between the filler and the polymer matrix [19,20]. However, the $\tan \delta$ values of the composites are unsatisfactory due to excessive current leakage arising from the formation of conductive pathways after reaching the percolation [21], prompting the need of solutions for suppressed leakage currents.

The use of electrically insulating two-dimensional (2D) materials such as boron nitride nanosheets (BNNS) as filler in polymer composites can prevent the leakage currents from developing by electrical conduction to lower the $\tan \delta$ and improve the E_b [1,10,20,22]. Compared to the bulk form of hexagonal boron nitride (h-BN), BNNS of large size ($\geq 2 \mu\text{m}$) with a mono or few-atomic-layer thickness are a preferred choice because of their high E_b of $\sim 800 \text{ MVm}^{-1}$ [23], excellent thermal conductivity (TC) of over $360 \text{ Wm}^{-1}\text{K}^{-1}$ [24], and high-temperature stability [25]. However, using BNNS alone cannot satisfy the requirement of high k values due to their relatively low k below 4 [22], and indeed, the reported dielectric performance of BNNS composites is only unsatisfactory [26]. Moreover, to achieve TCs of composites ranging from 1 to $10 \text{ Wm}^{-1}\text{K}^{-1}$, a high BNNS content of over 30 wt.% is usually required, compromising the dielectric performance of composites for practical applications [27]. In fact, such high TCs could easily be realized with less than 10 wt.% graphene fillers that possess larger aspect ratios and much higher TCs ($>2000 \text{ Wm}^{-1}\text{K}^{-1}$) than BNNS [28]. In addition, the inclusion of graphene can give rise to a drastically improved k of composites. However, the concurrent increase in electrical conductivity (EC) means an undesirable surge in $\tan \delta$, unable to employ polymer composites containing graphene fillers for dielectric applications [29]. Thus, designing electrically insulating composites with high k and low $\tan \delta$ is very challenging yet highly desirable for achieving high-performance dielectrics, for example, by taking advantage of electrically insulating BNNS and electrically conducting graphene as hybrid fillers in polymer composites.

With the foregoing backdrop in mind, this work reports the development of composites consisting of PVDF as matrix, and reduced graphene oxide (rGO) and BNNS as reinforcing fillers that can deliver excellent dielectric performance [30]. PVDF is chosen for its E_b and a relatively high k combined with a high energy density compared to other dielectric polymers [14]. The addition of rGO is designed to enhance the k through charge accumulation at the interfaces [19], while BNNS help suppress the $\tan \delta$ by preventing the mobility of free electrons along the conduction pathways [1]. Both nanofillers possess excellent TCs [31]. The microlaminate composites designed in this work consist of alternating rGO/PVDF and BNNS/PVDF layers such that both high k and low $\tan \delta$ values are achieved along with high E_b , charge energy densities, and TCs. The effects of number of alternating layers of electrically conducting and insulating composite films on dielectric performance are specifically studied.

2. Materials and Methods

2.1. Synthesis of rGO and BNNS

Graphene oxide (GO) was prepared using the modified Hummers' method established previously [32], which is particularly suitable for synthesizing large GO sheets from natural graphite (supplied by Asbury Graphite Mills, Asbury, NJ, USA). In brief, 3 g of expanded graphite (EG) powder was dispersed in H_2SO_4 ($>95\%$, Fisher Scientific, Waltham, MA, USA) and H_3PO_4 (85%, VWR Chemicals, Radnor, PA, USA) at a ratio of 360 to 40 mL. Then, 18 g of KMnO_4 ($\geq 99\%$, Fluka, St. Gallen, Switzerland) was slowly added to the mixture, followed by magnetic stirring at 40°C for 5 h. Afterward, the temperature was raised to 50°C and the mixture was stirred for another 12 h before cooling down to room temperature. Next, 400 mL ice of deionized (DI) water was poured into the mixture, followed by adding 5 mL H_2O_2 (30%, Honeywell, Charlotte, NC, USA), yielding yellowish-brown GO suspension. The GO suspension was washed with 10% dilute HCl solution (37%, VWR Chemicals)

on a centrifuge (Z326) at 12,000 rpm for 30 min which was repeated three times, followed by washing with DI water using the same centrifugation condition for three rounds. The collected GO was then reduced using hydrazine solution (N_2H_4 , 35 wt.% in H_2O , Sigma-Aldrich, St. Louis, MI, USA). Next, 0.5 mL GO was added to 5 mL H_2O and 5 μL N_2H_4 in a vial and stirred at 95 °C for 1 h. Then, 35 μL NH_4OH (Uni-chem) was added to maintain the pH of the mixture at around 9–10 during the reduction process. A black precipitate was obtained, which was subsequently dried (Scientz-10N) at -50 °C for 24 h to yield rGO sheets.

Bulk h-BN powders (99.5%, 325 mesh, supplied by Alfa Aesar, Haffrey, MA, USA) were exfoliated to form a few-layer BNNS using a planetary ball-mill (DECO, 1617003) [10] at an h-BN to urea ($\geq 99.0\%$, ACS, Washington, DC, USA) weight ratio of 1:30, operating at 400 rpm for 36 h. The urea had the following important functions: (i) aiding exfoliation of BNNS from the bulk h-BN; (ii) lubricating the milling balls to prevent BNNS from excessive mechanical damage; and (iii) functionalizing the BNNS to improve its dispersibility in polymer and solvent [10,33]. The milled product was diluted in DI water and washed several times by centrifugation, initially at 1000 rpm for 30 min to remove un-exfoliated thick h-BN sheets followed by washing of the supernatant at 12,000 rpm. The resultant BNNS were freeze-dried and collected for characterization and composite fabrication.

2.2. Fabrication of rGO/BNNS-PVDF Microlaminate Composites

To prepare hybrid composites, films consisting of individual fillers (BNNS/PVDF and rGO/PVDF) were first prepared, followed by a hot pressing and folding process [34]. PVDF (Sigma-Aldrich, $M_w \sim 534,000$ GPC powder) was dissolved in *N,N*-dimethylformamide (DMF, GC-99.8%, RCL Labscan, Bangkok, Thailand) solvent by magnetic stirring at 40 °C until a clear solution was formed. Then, the as-prepared BNNS fillers of varied weight fractions ranging from 10 to 30 wt.% were dispersed in DMF, which was mixed with PVDF solution by ultrasonication and stirring for 4 h to form a stable suspension. The suspension was cast onto a glass slide mold and dried in a vacuum oven (Mettler, 0173681). The as-prepared BNNS/PVDF films were collected from the mold after evaporating the solvent at 80 °C for 3 h. The BNNS/PVDF composite films are denoted as BN10, BN20, and BN30 according to their weight fractions. Similarly, rGO/PVDF films were prepared by dispersing rGO particles of different weight fractions ranging from 1 to 10 wt.% in DMF before mixing with PVDF solution. The rGO/PVDF composite films are denoted as rGO1, rGO3, rGO5, and rGO10 according to the weight fractions of rGO. Bilayer hybrid filler composites were prepared by stacking each of the BNNS/PVDF and rGO/PVDF composite films and pressing at 170 °C and ~ 3 MPa, which are designated as G/BNXX where XX stands for the weight fraction of BNNS in the BNNS/PVDF film. Here, G refers to the 10 wt.% rGO/PVDF composite which was selected for further study after preliminary experiments. Thereafter, the bilayer composites were subjected to folding and pressing at 170 °C and 3 MPa to form hybrid microlaminate composites of G/BNXX_YY with different total numbers of layers, where YY = 4, 8, 16, and 32 layers. A schematic of BNNS exfoliation and fabrication of hybrid microlaminate composites is shown in Figure 1, while the details of their designations and the corresponding filler weight fractions, number of layers, and thicknesses are presented in Table S1.

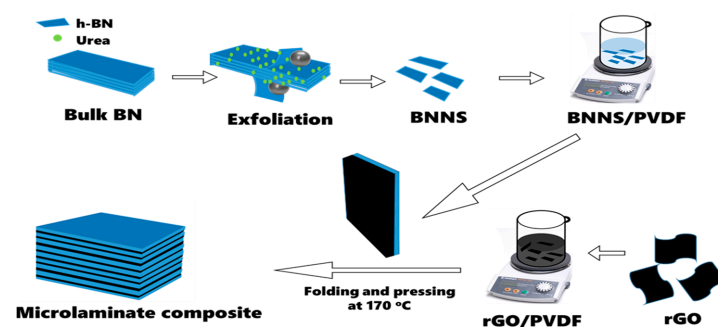


Figure 1. Schematic of BNNS exfoliation and fabrication procedure of microlaminate composites.

2.3. Characterization

The morphologies of h-BN, BNNS, and the cryo-fractured surface of the composites were characterized on a scanning electron microscope (SEM, JEOL JSM 6390) at an acceleration voltage of 20 kV. Raman spectroscopy (Reinshaw microRaman) was used to examine h-BN before and after exfoliation. The bonding characteristics and functional groups on BNNS before and after exfoliation were examined using the FTIR spectroscopy (Bruker Vertex 70Hyperion 1000) at wavelengths ranging from 400 cm^{-1} to 4000 cm^{-1} . The crystallization of bulk h-BN and BNNS was studied on an X'pert Pro (PANalytical) diffractometer with Cu K α ($\lambda = 0.154\text{ nm}$) radiation. The dielectric properties of the composites and neat PVDF were measured at room temperature using a precision LCR meter (E4980A) in the frequency range from 100 Hz to 1 MHz according to the specification, ASTM D150. The breakdown voltage of composites was measured using a Gamma high-voltage (HV) power supply (Model No-RR20-30R/220). Briefly, an electrode of $1\text{ cm} \times 1\text{ cm}$ in size was connected to the HV power source and placed in contact with both sides of the samples. Afterwards, the voltage was increased in a stepwise manner until the samples were mechanically failed. The breakdown strength was calculated by dividing the breakdown voltage by the sample thickness. The TC of composites was measured using a TPS 2500S hot disk. Three samples were tested for each set of conditions for the dielectric property, breakdown voltage, and TC measurements.

3. Results and Discussion

3.1. Exfoliation of BNNS

The exfoliation of h-BN is challenging due to the strong lip–lip interactions between its interlayers [35]. However, several methods have been explored to exfoliate h-BN into ultrathin BNNS. Among them, ball milling has proven to be effective, less time-consuming, giving rise to the highest yield of BNNS [33,36], making the technique attractive for adoption in this study. To minimize potential structural damage to BNNS due to high-speed ball collision during milling, a relatively low milling speed of 400 rpm was chosen, and urea [10] was added in the ball milling chamber to serve as intercalant and lubricant during exfoliation. The urea molecules helped reduce the effect of ball collision by adsorbing onto the h-BN surfaces and enlarged the interlayer spacing by intercalation of h-BN layers for easy exfoliation of BNNS. Figure S1a,b present bulk h-BN platelets of large thicknesses and varying lateral sizes and BNNS obtained after exfoliation, respectively. The AFM image and the corresponding height profile given in Figure S1c,d indicate that the BNNS had a lateral size of $\sim 2\text{ }\mu\text{m}$ and a thickness ranging from 7 to 10 nm. This implies that the impact of ball collision was mild and did not cause severe fragmentation of h-BN into smaller pieces during exfoliation. The XRD patterns shown in Figure S1e exhibit a prominent (002) peak at $2\theta = 26.93^\circ$ with a d-spacing of 3.308 for h-BN. After exfoliation, its intensity was significantly reduced and the peak position was downshifted to $2\theta = 26.79^\circ$ giving rise to a larger d-spacing of 3.324, which is consistent with previous findings [1]. In addition, the intensities of other minor diffraction peaks of the (100), (101), (102), (004), (104), and (110) planes were reduced after exfoliation, while no urea peak was identified. The intensity ratio of the (100) to (004) plane peaks, $I_{(100)}/I_{(004)}$, decreased from 0.64 to 0.30 after exfoliation, which signifies the alignment of BNNS in the horizontal plane as a result of their high aspect ratios [1,37]. The thickness of BNNS on the crystalline plane (002) at 26.79° was calculated to be 9.93 nm according to the Debye–Scherrer equation: $t = \frac{K\lambda}{FWHM \cdot \cos\theta}$, where FWHM is the full width at half maximum, θ is the peak position, λ is the wavelength of X-ray, and K is the shape factor. This value falls within the thickness range measured from the AFM findings.

The Raman spectra of h-BN and BNNS shown in Figure S1f exhibit noticeable G-band peaks at 1365 cm^{-1} and 1366 cm^{-1} , respectively, corresponding to the E_{2g} mode vibration. The marginal upshift of the peak after exfoliation indicates weaker interlayer interactions in BNNS, which corroborates the enlarged d-spacing [1]. There was significant broadening of the G-band peak of BNNS after exfoliation with an increase in FWHM from

11.7 to 13.0, which is attributed to stronger surface scattering influencing the vibrational excitation [35,38]. Their chemistry and bonding characteristics were analyzed using the FTIR spectra. Both materials exhibited similar bond characteristics at ~ 759 and ~ 1375 cm^{-1} , as shown in Figure S1g, corresponding to the B-N in-plane bending and B-N out-of-plane stretching vibrations, respectively. However, additional broad band peaks appeared at 3221 and 3406 cm^{-1} for BNNS, corresponding to the N-H stretching and O-H stretching, respectively. The former indicates the functionalization of BNNS by urea, while the latter reflects the effect of centrifugal washing after ball milling.

3.2. Structure and Dielectric Properties of Microlaminate Composites

To understand the contributions from the individual fillers to the dielectric performance of hybrid filler composites, laminates were fabricated by initially stacking two films with different filler types followed by folding and pressing. The folding technique was used simply because it is more convenient than the direct stacking approach and there is no need to cut the composites into pieces at high temperature before stacking. In addition, the technique is effective in controlling the distribution of fillers and builds up multiple alternating layers in the microlaminate composites so that an optimal structural configuration can be identified. Typically, composites with high 2D nanofiller loadings often encounter difficulties of uniform dispersion due to the high tendency of agglomeration of these fillers, resulting in severely deteriorated mechanical, physical, and dielectric performance of the composites.

The folding and pressing process was carried out at 170 °C below the melting point of PVDF after trial-and-error experiments to avoid both complete fusion of the layers and thus disruption of filler orientation in the in-plane direction. Figure 2a presents the SEM image of G/B30 bilayer composite consisting of an electrically insulating BNNS/PVDF layer firmly bonded together with an electrically conducting rGO/PVDF layer. The composite of four layers (G/B30_4L) was prepared by folding the G/B30 film such that the BNNS/PVDF films formed the outer layers, while the two layers of rGO/PVDF film were stacked as inner layers. The same process was repeated until the 32-layer microlaminate composite containing 16 layers each of rGO/PVDF and BNNS/PVDF films was obtained, as schematically shown in Figure 2b. It is worth mentioning that the hot-pressing process made the nanofiller distribution within each layer highly aligned, as shown in Figure 2c,d.

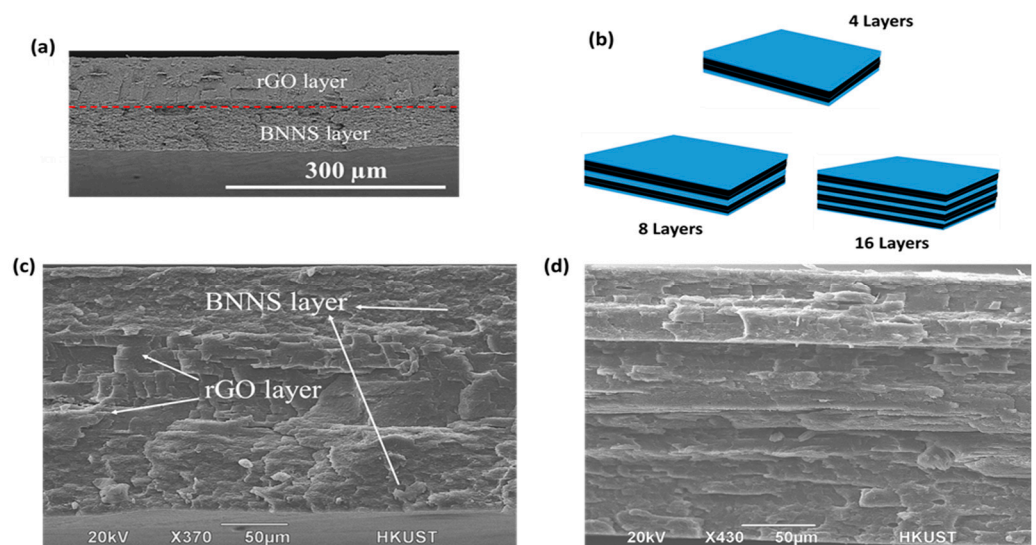


Figure 2. (a) SEM image of cryo-fractured edge surface of G/B30 bilayer composite. (b) Schematics of 4, 8, and 16-layer microlaminate composites; the blue and black layers represent the BNNS/PVDF and rGO/PVDF composite films, respectively. (c,d) SEM image of cryo-fractured edge surface of respective 4 and 32-layer microlaminate composites.

In the preliminary experiments, the effects of individual fillers on dielectric properties and electrical conductivities of the composites were investigated. The k and $\tan \delta$ curves of neat PVDF, BNNS/PVDF, and rGO/PVDF single-layer composite films and G/B bilayer composites plotted as a function of frequency are shown in Figure S2, and the k and $\tan \delta$ values measured at a frequency of 1 kHz are summarized in Figure 3a,c,d. As shown in Figure 3a, both the k and $\tan \delta$ of BNNS/PVDF composites gradually decreased as the BNNS wt.% increased, even below the neat PVDF counterparts, due to the insulating nature of BNNS fillers in the PVDF matrix. Conversely, the k of rGO/PVDF composites drastically increased after the incorporation of rGO fillers of above 5 wt.% and reached the highest value of 628 at 10 wt.% due to the formation of percolating network by the highly conducting rGO sheets. This finding is consistent with the electrical conductivity shown in Figure 3b where the composites with rGO filler content higher than 5 wt.% behaved like a conductor. The Maxwell–Wagner–Sillars (MWS) effect explains the interfacial polarization, which was induced by charge entrapment in the composite because of the inclusion of conducting rGO sheets. Despite showing a great potential for high energy storage capacities due to their high k values [19], the rGO/PVDF composites alone cannot be used for meaningful applications because of their high $\tan \delta$ values, far above the practically viable level of 0.1 [10].

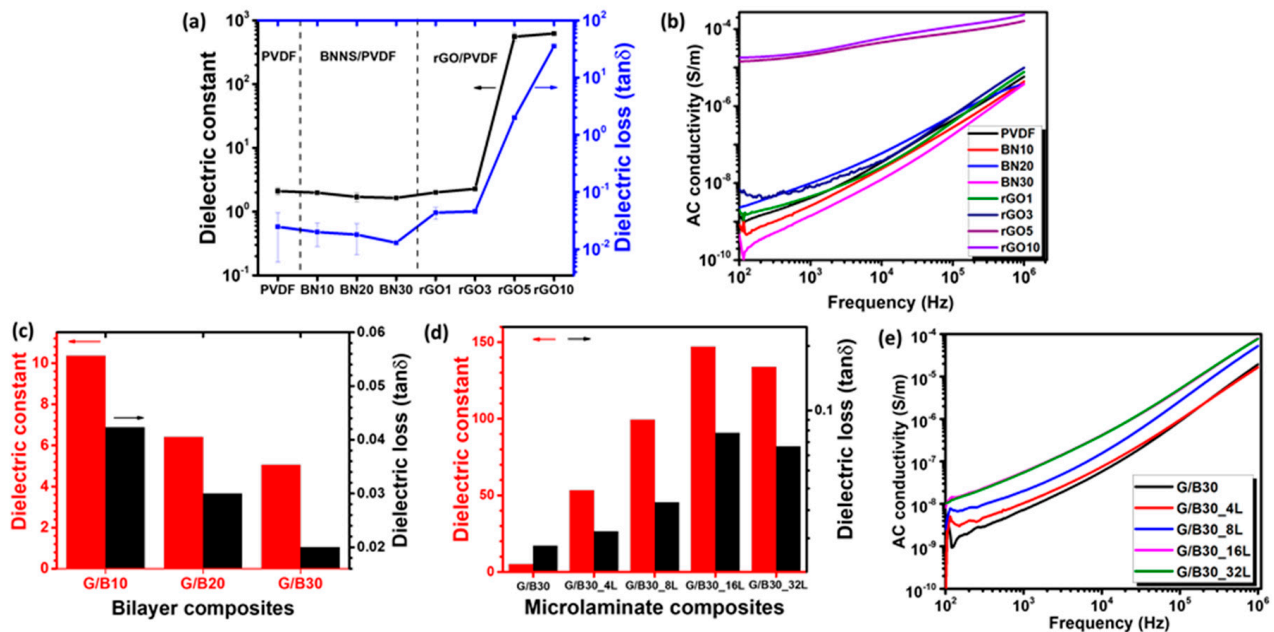


Figure 3. (a) Dielectric constant and loss at 1 kHz and (b) AC conductivity of PVDF, rGO/PVDF, and BNNS/PVDF films. (c) Dielectric constant and loss at 1 kHz of bilayer composites. (d) Dielectric constant and loss at 1 kHz and (e) AC conductivity of microlaminate composites comprising different numbers of rGO/PVDF and BNNS/PVDF films.

In an attempt to simultaneously achieve high k and low $\tan \delta$ values, hybrid composites were fabricated by alternately stacking conducting rGO/PVDF and insulating BNNS/PVDF films. Initially, a single layer of the BNNS/PVDF composite containing varying BNNS contents was stacked on top of a single layer of the rGO10 composite to form bilayer composites, designated as G/B10, G/B20, and G/B30. The rGO10 composite was selected to ensure that the rGO filler content of bilayer composites was 5 wt.%. The dielectric properties of bilayer composites are shown in Figure S2 and Figure 3c. While their $\tan \delta$ values were sufficiently low, the absolute k values ranged from 5.1 to 10.4, much enhanced compared to the neat PVDF or all BNNS/PVDF and rGO1, rGO3 composite counterparts, due to the synergy arising from the presence of both the electrically insulating and conducting layers. It is also worth noting that both the k and $\tan \delta$ deteriorated with in-

creasing BNNS content, indicating that the BNNS dominated the dielectric performance of bilayer composites such as the single-layer BNNS/PVDF film (Figure 3a). Given the lowest $\tan \delta$ of 0.02, the G/B30 bilayer composite was chosen to fabricate alternating multilayer structures, and their dielectric properties are plotted as a function of frequency in Figure S3 and the results are summarized in Figure 3d. Interestingly, the k of the multilayer microlaminate composites increased significantly as the number of rGO/PVDF layers increased with a simultaneous increase in $\tan \delta$, but within the acceptable range below 0.1 [10]. The k augmented from ~ 5.1 of the bilayer composite (G/B30) to ~ 147 of the 16-layer microlaminate (G/B30_16L), whereas the corresponding $\tan \delta$ increased to ~ 0.08 when measured at 1 kHz. Due to the large differences in conductivity and dielectric performance between the rGO/PVDF and BNNS/PVDF films, the effect of MWS interfacial polarization became more conspicuous when increasing the number of layers, which was mainly responsible for the surge in dielectric constant. The result also shows that the 32-layer microlaminate composite displayed a slightly lower k of ~ 140 than the 16-layer microlaminate counterpart and a marginally lower $\tan \delta$ of 0.07. This observation is probably associated with the sliding caused by composite layer infusion at a higher number of layers during the hot press process [39,40]. It also implies that the microlaminate composite consisting of numerous micro-capacitors of rGO/PVDF and BNNS/PVDF layers became affected by the inhomogeneous boundaries as a result of uneven loading, thereby degrading the dielectric constant. The lower AC conductivities of the microlaminate composites than the rGO5 and rGO10 counterparts, as shown in Figure 3e, further suggest the generally insulating nature of the composites, which is ascribed to the multiple insulating BNNS/PVDF layers, suppressing the $\tan \delta$ below 0.1.

Figure 4a shows the average breakdown strength E_b of the composites calculated according to the specification, ASTM Standard D149-09 [41]. The bilayer and microlaminate composites had excellent E_b up to a maximum of 97.8 and 78.4 MV/m, respectively, about 16 and 13 times that of the rGO10 composite acting alone without BN30 insulating films. The inherently high breakdown strength of BN30 composites—about 287.2 MV/m—and its excellent insulating barrier characteristics among the rGO10 layers contributed to the enhanced breakdown strengths of the bilayer and microlaminate composites. As expected, with increasing the filler content, the E_b of monolayer BNNS/PVDF composites increased, whereas that of monolayer rGO/PVDF composites decreased. A similar trend was observed for bilayer composites whereby the E_b increased as the BNNS wt.% increased. However, among the microlaminates, the composite with four layers showed the highest E_b value of 78.4 MV/m, which decreased as the number of layers increased to 56.4 MV/m for a 16-layer composite, except for a 32-layer composite, which showed a higher E_b value of 75 MV/m. The multilayer laminates containing the same BNNS and rGO contents presented slightly lower E_b than the bilayer counterpart. In this case, the E_b was adversely affected by the thicker composite laminates than the bilayer composites. The observation also indicates that one thick film of strong BN30/PVDF in the bilayer composite was able to withstand the applied electric field better than the multiple BN30/PVDF films sandwiched by weak rGO10/PVDF films in the multilayer microlaminates. The dielectric breakdown mechanism is schematically presented in Figure S4, where the electrical tree or conduction pathway (indicated by the red arrows) in the polymer matrix was responsible for the composites to breakdown under an applied voltage field [42]. In other words, the hindrance of electrical tree growth by the insulating BNNS fillers as well as the layered structure translates to a better breakdown strength exhibited by the microlaminate composites when compared to monolayer rGO/PVDF counterparts.

The energy stored in a dielectric capacitor can be expressed in terms of electric field (E_f) and electric displacement (D) as $U_e = \int E_f dD$. However, for linear dielectric materials whose dielectric constant is not dependent on the external electric field, the energy stored (U_e) can be further expressed as: $0.5\varepsilon_0 k E_b^2$, where ε_0 ($=8.85 \times 10^{-12} \text{ Fm}^{-1}$) is the dielectric constant of vacuum. In Figure 4b, the energy density of the microlaminate composites improved with increasing the number of layers. The G/B30_32L composite had the highest

value of 3.5 J/cm^3 , which is about 6 and 35 times those of the BN30 and rGO10 single-filler composites, respectively. The value is even higher than that of the conventional dielectric, biaxially oriented polypropylene (BOPP), for energy storage applications [13]. Although the microlaminate composite delivered a relatively lower dielectric constant than rGO10 and a lower breakdown strength than BN30, it had great energy storage potential compared to these single-filler composites acting alone. This finding emphasizes the importance of striking a balance between dielectric constant, dielectric loss, and breakdown strength to achieve an optimized energy density of composites. In summary, the high energy density of the microlaminate composites recorded in this work can be attributed to the synergy arising from the alternately layered architecture of conducting rGO/PVDF and insulating BNNS/PVDF films, which contributes to its relatively high dielectric constant and well-suppressed dielectric loss and high breakdown strength.

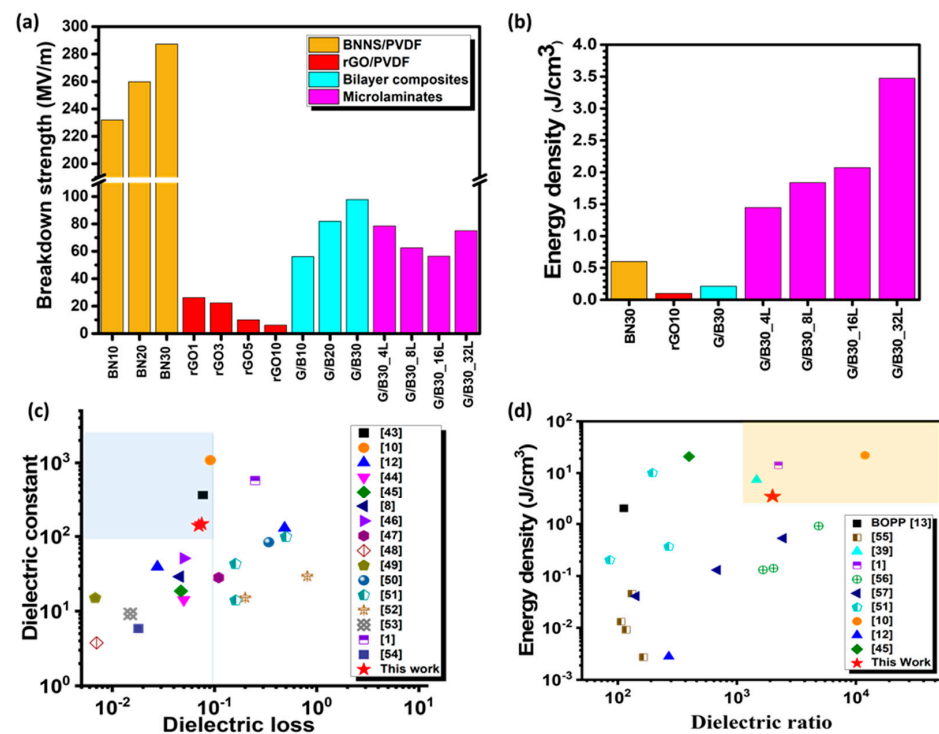


Figure 4. (a) Breakdown strength of rGO/PVDF, BNNS/PVDF, bilayer, and microlaminate composites. (b) Energy density of single-layer, bilayer, and microlaminate composites. (c) Comparison of dielectric constant versus dielectric loss and (d) energy density versus dielectric ratio among the current microlaminate composite and other rGO- and/or BNNS-based polymer composites reported in the literature. The light-blue region in (c) and light-orange region in (d) are considered ideal ranges of properties for dielectric composites.

The dielectric performance and energy density of selected microlaminate composites are compared with those of the dielectric composites reported in the open literature as shown in Tables 1 and 2 [1,8,10,12,39,43–57], and the summary comparisons are plotted in Figure 4c,d. Given the counteracting characteristics between dielectric constant and dielectric loss, the dielectric ratio—the ratio of dielectric constant to dielectric loss—is considered as a basis for comparison to measure the overall dielectric performance of the composites. It can be seen that the microlaminate composites reported in this work possess dielectric performance highly competitive with reported values or even better than the majority, indicating that the design approach and the method adopted for fabricating the microlaminate composites are sensibly demonstrated for high dielectric constants and suppressed dielectric losses for emerging energy storage applications.

Table 1. Comparison of dielectric constants and losses of our microlaminate composites with other composites reported in the literature.

Materials	At 1 kHz		Ref.
	Dielectric Constant	Dielectric Loss (tan δ)	
BaTiO ₃ /Graphite/PDMS	73.5	0.19	[43]
rGO-PU/BN-PU	1084	0.091	[10]
BT@HBP/PMMA-4	130	0.485	[12]
BT@HBP@PMMA-4	39.3	0.0276	[12]
PVDF/Mxene@CTAB	82.1	0.2	[44]
PVDF/P(VDF-TrFE-CTFE)/PVDF	18.61	0.047	[45]
Mxene/PVDF	29	0.046	[8]
rGO-TiO ₂ /PVDF	211	0.104	[46]
PVDF/hBN/SiC	28.1	0.11	[47]
mBN/PI	3.77	0.007	[48]
epoxy/h-BN/rGO	15	0.0068	[49]
SMG/PVDF	83.8	0.34	[50]
	98.91	0.501	
GROH/PVDF	42.9	0.16	[51]
	13.91	0.161	
	29.4	0.81	
FGS/PP	15.2	0.2	[52]
Ag-PDOP/PVDF	9.2	0.015	[53]
rGO-PI/BNNS-PI	579	0.25	[1]
BN/CNT/PVDF	5.86	0.018	[54]
	147.1	0.075	
G/B30_16L	139.5	0.07	This work

PDMS: polydimethylsiloxane; HBP: hyperbranched aromatic polyamide; BT: barium titanate; GROH: hydroxylated graphene; CTAB: cetyltrimethylammonium bromide; P(VDF-TrFE-CTFE): poly(vinylidene fluoride-ter-trifluoroethylene-ter-chlorotrifluoroethylene); SMG: surface-modified graphene; FGS: functionalized graphene sheets; PP: polypropylene; Ag-PDOP: silver-polydopamine.

Table 2. Comparison of energy density as a function of dielectric ratio of our microlaminate composites with other composites reported in the literature.

Materials	Dielectric Ratio	Energy Density (J/cm ³)	Ref.
	164	0.0027	
	117	0.0092	
GO/CNT/PU	107	0.013	[55]
	131	0.046	
	1656	0.13	
PPD-CFGO/PI	2030	0.14	[56]
	4857	0.91	
	143	0.041	
Dopamine@BCZT/PVDF	684	0.13	[57]
	2446	0.53	
	86	0.20	
GROH/PVDF	268	0.37	[51]
	196	10.07	
	11912	22.70	[10]
rGO-PU/BN-PU	1464	7.40	[39]
Mxene/PVDF	268	0.0028	[12]
BT@HBP/PMMA-4	396	20.86	[45]
PVDF/P(VDF-TrFE-CTFE)/PVDF	2316	14.20	[1]
rGO-PI/BNNS-PI	1993	3.50	This work
G/B30_32L			

PPD: *p*-Phenylenediamine; CFGO: carboxyl-functionalized GO; BCZT: calcium barium zirconate titanate (Ba_{0.95}Ca_{0.05}Zr_{0.15}Ti_{0.85}O₃).

3.3. Thermal Properties of the Composites

Although the microlaminate composites showed a good dielectric performance, it is important to investigate their TC for multifunctional applications because dielectric materials must also withstand and effectively dissipate heat during service. While

polymer-based dielectrics are attractive for miniaturizing electrical storage devices, their low TC values are often a major setback for practical applications [54]. It is not uncommon for dielectric materials to exhibit a conduction loss phenomenon where the dielectric loss is converted into heat during service. Unless the heat is properly removed, early breakdown of the material may take place [20]. Figure 5a shows the TC of selected single-layer and bilayer composites as well as microlaminate composites. It is shown that both the single-layer and bilayer composites showed an improved TC compared to the neat PVDF. The TC of the microlaminates increased almost linearly with increasing the number of constituent layers, reaching the highest value of $6.53 \text{ Wm}^{-1}\text{K}^{-1}$ for the 32-layer composite, which is equivalent to 38-, 27-, and 13-fold enhancement compared to the neat PVDF ($0.17 \text{ Wm}^{-1}\text{K}^{-1}$), single-layer and bilayer composites, respectively. Aside from the inherently high TCs of rGO and BNNS, the remarkable TC enhancement, especially for the composites consisting of a large number of layers, is attributed to the better alignment of 2D fillers in the plane direction. Figure 5b and Table 3 [1,9,20,26,27,49,54,58–60] compare the TCs of the current microlaminate and state-of-the-art values reported for other rGO and BNNS polymer composites, presenting a relatively high TC value for the microlaminates when the filler content is taken into account.

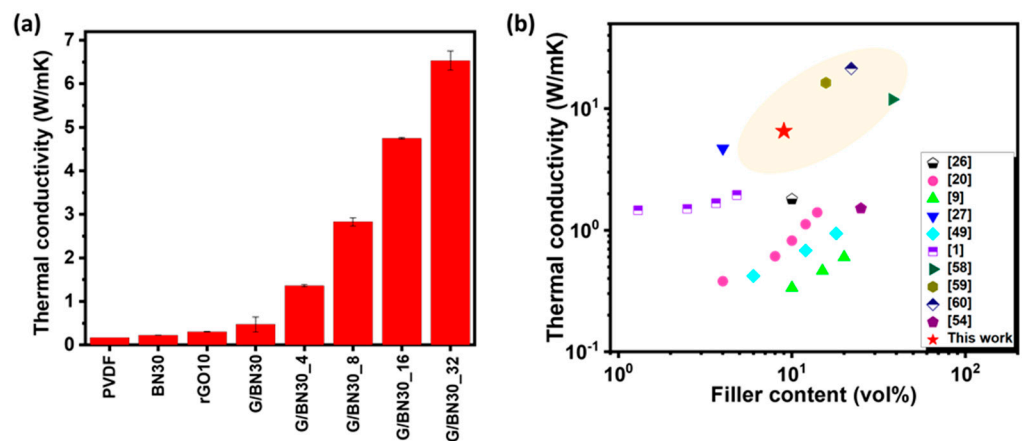


Figure 5. (a) Thermal conductivities of neat PVDF, single-layer, bilayer, and microlaminate composites. (b) Comparison of thermal conductivities among the current microlaminate composite and other rGO- and/or BNNS-based polymer composites reported in the literature.

Table 3. Comparison of thermal conductivities of our microlaminate with other rGO and/or BNNS polymer composites reported in the literature.

Materials	Filler Content (Vol%)	Thermal Conductivity ($\text{Wm}^{-1}\text{K}^{-1}$)	Ref.
c-BCB/BNNS	10	1.80	[26]
GO/BNNS/PVA	38.01	11.90	[58]
BNNS/P(VDF-TrFE-CFE)	14	1.40	[20]
	8	0.61	
BNNS/epoxy	20	0.60	[9]
	10	0.34	
BNNS/PVDF	15.71	16.30	[59]
BNNS/PVA	22	21.40	[60]
BNNS/PVDF	4	4.69	[27]
BNNS/rGO/epoxy	18	0.94	[49]
rGO-PI/BNNS-PI	1.30	1.49	[1]
	4.82	1.95	
m-h-BN/MWCNTs-SiO ₂ /PVDF	25	1.51	[54]
G/B30_32L	10	6.53	This work

c-BCB: crosslinked divinyltetramethyldisiloxane-bis(benzocyclobutene); PVA: polyvinyl alcohol; MWCNTs: multi-walled carbon nanotubes.

4. Conclusions

This work demonstrates simultaneous achievement of high dielectric constants and ultralow dielectric losses of hybrid composites made by electrically conducting reduced graphene oxide (rGO) and electrically insulating boron nitride nanosheets (BNNS) fillers in a PVDF matrix via a folding and pressing process to form an alternating multilayer microlaminate composite. The microlaminate composite assembled with 16 layers each of rGO/PVDF and BNNS/PVDF films delivered a maximum dielectric constant of 140 and an ultralow dielectric loss of ~ 0.07 at 1 kHz, as well as a high energy density of 3.5 J/cm^3 . The remarkable dielectric performance of the composite was attributed to the synergy arising from the hybrid fillers of BNNS and rGO, as well as the alternating multilayer structure. The electrically conducting rGO/PVDF layers helped augment the dielectric constant, while the electrically insulating BNNS/PVDF layers suppressed the leakage currents to reduce the dielectric loss and improve the breakdown strength. Furthermore, the microlaminate composite exhibited an excellent thermal conductivity of $6.53 \text{ Wm}^{-1}\text{K}^{-1}$, arising from the highly thermally conducting fillers and their significant alignment during the pressing and folding process, thereby allowing efficient heat transport along the in-plane direction. The rational design of layer-structured laminates through the folding and pressing approach developed in this work will offer new insights into the achievement of high dielectric performance for high energy storage applications of rGO and BNNS hybrid polymer composites.

Supplementary Materials: The following supporting information can be downloaded at: <https://www.mdpi.com/article/10.3390/nano12244492/s1>, Figure S1: Morphology, structure, and chemistry of bulk BN and BNNSs. (a,b) SEM images, (c,d) AFM image and the corresponding height profile of BNNS. (e) XRD patterns, (f) Raman spectra and (g) FTIR spectra of bulk BN and BNNS; Figure S2: (a,c,e) Dielectric constant (k) and (b,d,f) dielectric loss ($\tan \delta$) of neat PVDF, BNNS/PVDF, and rGO/PVDF single-layer composite films and G/B bilayer composites as a function of frequency ranging from 10^2 to 10^6 Hz; Figure S3: (a) Dielectric constant (k) and (b) dielectric loss ($\tan \delta$) of microlaminate composites with different number of layers as a function of frequency ranging from 10^2 to 10^6 Hz; Figure S4: Schematic of electrical pathways in composites; Table S1: Designations of composite materials prepared in this work.

Author Contributions: Conceptualization, O.G.A.; methodology, O.G.A., H.Z. and M.H.A.; writing—original draft preparation, O.G.A.; writing—review and editing, O.G.A., M.H.A., K.-Y.C., H.Z., X.S. and J.-K.K.; supervision, J.-K.K. and X.S.; project administration, J.-K.K.; funding acquisition, X.S. and J.-K.K. All authors have read and agreed to the published version of the manuscript.

Funding: This research was funded by “Research Grants Council (GRF Projects: 16205517, 16209917 and 16200720)” and “Innovation and Technology Commission (ITS/012/19) of Hong Kong SAR”.

Data Availability Statement: Not applicable.

Acknowledgments: O.G.A. and M.H.A. are recipients of the Hong Kong PhD Fellowship. Technical assistance from the Advanced Engineering Materials Facilities (AEMF), Materials Characterization and Preparation Facilities (MCPF), and the Department of Electronic and Computer Engineering (Allen NG) at HKUST are appreciated.

Conflicts of Interest: The authors declare no conflict of interest.

References

1. Guo, F.; Shen, X.; Zhou, J.; Liu, D.; Zheng, Q.; Yang, J.; Jia, B.; Lau, A.K.; Kim, J.K. Highly thermally conductive dielectric nanocomposites with synergistic alignments of graphene and boron nitride nanosheets. *Adv. Funct. Mater.* **2020**, *30*, 201910826. [[CrossRef](#)]
2. Zhang, C.; Shi, Z.; Mao, F.; Yang, C.; Yang, J.; Zhu, X.; Zuo, H. Polymer composites with balanced dielectric constant and loss via constructing trilayer architecture. *J. Mater. Sci.* **2018**, *53*, 13230–13242. [[CrossRef](#)]
3. Korolkov, I.V.; Zhumanazar, N.; Gorin, Y.G.; Yeszhanov, A.B.; Zdorovets, M.V. Enhancement of electrochemical detection of Pb^{2+} by sensor based on track-etched membranes modified with interpolyelectrolyte complexes. *J. Mater. Sci. Mater. Electron.* **2020**, *31*, 20368–20377. [[CrossRef](#)]

4. Yakovenko, O.; Lazarenko, O.; Matzui, L.; Vovchenko, L.; Borovoy, M.; Tesel'ko, P.; Lozitsky, O.; Astapovich, K.; Trukhanov, A.; Trukhanov, S. Effect of Ga content on magnetic properties of BaFe₁₂–xGa_xO₁₉/epoxy composites. *J. Mater. Sci.* **2020**, *55*, 9385–9395. [[CrossRef](#)]
5. Zdorovets, M.V.; Kozlovskiy, A.L.; Shlimas, D.I.; Borgekov, D.B. Phase transformations in FeCo–Fe₂CoO₄/Co₃O₄-spinel nanostructures as a result of thermal annealing and their practical application. *J. Mater. Sci. Mater. Electron.* **2021**, *32*, 16694–16705. [[CrossRef](#)]
6. Zhang, D.; Liu, W.; Guo, R.; Zhou, K.; Luo, H. High discharge energy density at low electric field using an aligned titanium dioxide/lead zirconate titanate nanowire array. *Adv. Sci.* **2018**, *5*, 1700512. [[CrossRef](#)]
7. Vinnik, D.A.; Zhivulin, V.E.; Sherstyuk, D.P.; Starikov, A.Y.; Zezyulina, P.A.; Gudkova, S.A.; Zherebtsov, D.A.; Rozanov, K.N.; Trukhanov, S.V.; Astapovich, K.A.; et al. Electromagnetic properties of zinc–nickel ferrites in the frequency range of 0.05–10 GHz. *Mater. Today Chem.* **2021**, *20*, 100460. [[CrossRef](#)]
8. Feng, Y.; Wu, Q.; Deng, Q.; Peng, C.; Hu, J.; Xu, Z. High dielectric and breakdown properties obtained in a PVDF based nanocomposite with sandwich structure at high temperature via all-2D design. *J. Mater. Chem. C* **2019**, *7*, 6744–6751. [[CrossRef](#)]
9. Donnay, M.; Tzavalas, S.; Logakis, E. Boron nitride filled epoxy with improved thermal conductivity and dielectric breakdown strength. *Compos. Sci. Technol.* **2015**, *110*, 152–158. [[CrossRef](#)]
10. Wu, Y.; Wang, Z.; Shen, X.; Liu, X.; Han, N.M.; Zheng, Q.; Mai, Y.W.; Kim, J.K. Graphene/boron nitride–polyurethane microlaminates for exceptional dielectric properties and high energy densities. *ACS Appl. Mater. Interf.* **2018**, *10*, 26641–26652. [[CrossRef](#)]
11. Sima, W.; Jiang, X.; Peng, Q.; Sun, P. Investigation of dielectric properties of polyethylene terephthalate under different aging temperatures. *IEEE Trans. Dielec. Electr. Insul.* **2017**, *24*, 3015–3023. [[CrossRef](#)]
12. Xie, L.; Huang, X.; Huang, Y.; Yang, K.; Jiang, P. Core@ double-shell structured BaTiO₃–polymer nanocomposites with high dielectric constant and low dielectric loss for energy storage application. *J. Phys. Chem. C* **2013**, *117*, 22525–22537. [[CrossRef](#)]
13. Hu, P.; Shen, Y.; Guan, Y.; Zhang, X.; Lin, Y.; Zhang, Q.; Nan, C.W. Topological-structure modulated polymer nanocomposites exhibiting highly enhanced dielectric strength and energy density. *Adv. Funct. Mater.* **2014**, *24*, 3172–3178. [[CrossRef](#)]
14. Thakur, V.K.; Gupta, R.K. Recent progress on ferroelectric polymer-based nanocomposites for high energy density capacitors: Synthesis, dielectric properties, and future aspects. *Chem. Rev.* **2016**, *116*, 4260–4317.
15. Selvaraj, M.; Senthilkumar, R.; Balaji, R.; Selvasekarapandian, S.; Manivasagam, T.G. Influence of graphene oxide and reduced graphene oxide on dielectric properties of PZT/PVDF composite films. *AIP Conf. Proc.* **2019**, *2162*, 020056.
16. Guo, R.; Luo, H.; Yan, M.; Zhou, X.; Zhou, K.; Zhang, D. Significantly enhanced breakdown strength and energy density in sandwich-structured nanocomposites with low-level BaTiO₃ nanowires. *Nano Energy* **2021**, *79*, 105412. [[CrossRef](#)]
17. Kozlovskiy, A.L.; Shlimas, D.I.; Zdorovets, M.V. Synthesis, structural properties and shielding efficiency of glasses based on TeO₂–(1-x) ZnO–xSm₂O₃. *J. Mater. Sci. Mater. Electron.* **2021**, *32*, 12111–12120. [[CrossRef](#)]
18. Almessiere, M.A.; Güner, S.; Slimani, Y.; Hassan, M.; Baykal, A.; Gondal, M.A.; Baig, U.; Trukhanov, S.V.; Trukhanov, A.V. Structural and magnetic properties of Co_{0.5}Ni_{0.5}Ga_{0.01}Gd_{0.01}Fe_{1.98}O₄/ZnFe₂O₄ spinel ferrite nanocomposites: Comparative study between sol-gel and pulsed laser ablation in liquid approaches. *Nanomaterials* **2021**, *11*, 2461. [[CrossRef](#)]
19. Yousefi, N.; Sun, X.; Lin, X.; Shen, X.; Jia, J.; Zhang, B.; Tang, B.; Chan, M.; Kim, J.K. Highly aligned graphene/polymer nanocomposites with excellent dielectric properties for high-performance electromagnetic interference shielding. *Adv. Mater.* **2014**, *26*, 5480–5487. [[CrossRef](#)]
20. Li, Q.; Zhang, G.; Liu, F.; Han, K.; Gadinski, M.R.; Xiong, C.; Wang, Q. Solution-processed ferroelectric terpolymer nanocomposites with high breakdown strength and energy density utilizing boron nitride nanosheets. *Energy Environ. Sci.* **2015**, *8*, 922–931. [[CrossRef](#)]
21. Dang, Z.M.; Zheng, M.S.; Zha, J.W. 1D/2D carbon nanomaterial-polymer dielectric composites with high permittivity for power energy storage applications. *Small* **2016**, *12*, 1688–1701. [[CrossRef](#)] [[PubMed](#)]
22. Zhu, Y.; Zhu, Y.; Huang, X.; Chen, J.; Li, Q.; He, J.; Jiang, P. High energy density polymer dielectrics interlayered by assembled boron nitride nanosheets. *Adv. Energy Mater.* **2019**, *9*, 1901826. [[CrossRef](#)]
23. Padilha, J.E.; Pontes, R.B.; Fazzio, A. Bilayer graphene on h-BN substrate: Investigating the breakdown voltage and tuning the bandgap by electric field. *J. Phys. Cond. Matter* **2012**, *24*, 075301. [[CrossRef](#)] [[PubMed](#)]
24. Wang, Z.; Tang, Z.; Xue, Q.; Huang, Y.; Huang, Y.; Zhu, M.; Pei, Z.; Li, H.; Jiang, H.; Fu, C.; et al. Fabrication of boron nitride nanosheets by exfoliation. *Chem. Record* **2016**, *16*, 1204–1215. [[CrossRef](#)] [[PubMed](#)]
25. Jo, I.; Pettes, M.T.; Kim, J.; Watanabe, K.; Taniguchi, T.; Yao, Z.; Shi, L. Thermal conductivity and phonon transport in suspended few-layer hexagonal boron nitride. *Nano Lett.* **2013**, *13*, 550–554. [[CrossRef](#)] [[PubMed](#)]
26. Li, Q.; Chen, L.; Gadinski, M.R.; Zhang, S.; Zhang, G.; Li, H.U.; Iagodkine, E.; Haque, A.; Chen, L.Q.; Jackson, T.N.; et al. Flexible high-temperature dielectric materials from polymer nanocomposites. *Nature* **2015**, *523*, 576–579. [[CrossRef](#)]
27. Wang, M.; Jiao, Z.; Chen, Y.; Hou, X.; Fu, L.; Wu, Y.; Li, S.; Jiang, N.; Yu, J. Enhanced thermal conductivity of poly(vinylidene fluoride)/boron nitride nanosheet composites at low filler content. *Compos. Part A Appl. Sci. Manuf.* **2018**, *109*, 321–329. [[CrossRef](#)]
28. Shahil, K.M.; Balandin, A.A. Graphene–multilayer graphene nanocomposites as highly efficient thermal interface materials. *Nano Lett.* **2012**, *12*, 861–867. [[CrossRef](#)]
29. Li, J.; Kim, J.K. Percolation threshold of conducting polymer composites containing 3D randomly distributed graphite nanoplatelets. *Compos. Sci. Technol.* **2007**, *67*, 2114–2120. [[CrossRef](#)]

30. Shen, X.; Zheng, Q.; Kim, J.K. Rational design of two-dimensional nanofillers for polymer nanocomposites toward multifunctional applications. *Prog. Mater. Sci.* **2021**, *115*, 100708. [[CrossRef](#)]
31. Yu, S.; Shen, X.; Kim, J.K. Beyond homogeneous dispersion: Oriented conductive fillers for high κ nanocomposites. *Mater. Horiz.* **2021**, *8*, 3009–3042. [[CrossRef](#)] [[PubMed](#)]
32. Lin, X.; Shen, X.; Zheng, Q.; Yousefi, N.; Ye, L.; Mai, Y.W.; Kim, J.K. Fabrication of highly-aligned, conductive, and strong graphene papers using ultralarge graphene oxide sheets. *ACS Nano* **2012**, *6*, 10708–10719. [[CrossRef](#)] [[PubMed](#)]
33. Lei, W.; Mochalin, V.N.; Liu, D.; Qin, S.; Gogotsi, Y.; Chen, Y. Boron nitride colloidal solutions, ultralight aerogels and freestanding membranes through one-step exfoliation and functionalization. *Nat. Commun.* **2015**, *6*, 8849. [[CrossRef](#)] [[PubMed](#)]
34. Santagiuliana, G.; Picot, O.T.; Crespo, M.; Porwal, H.; Zhang, H.; Li, Y.; Rubini, L.; Colonna, S.; Fina, A.; Barbieri, E.; et al. Breaking the nanoparticle loading–dispersion dichotomy in polymer nanocomposites with the art of croissant-making. *ACS Nano* **2018**, *12*, 9040–9050. [[CrossRef](#)]
35. Zhu, W.; Gao, X.; Li, Q.; Li, H.; Chao, Y.; Li, M.; Mahurin, S.M.; Li, H.; Zhu, H.; Dai, S. Controlled gas exfoliation of boron nitride into few-layered nanosheets. *Angew. Chem.* **2016**, *128*, 10924–10928. [[CrossRef](#)]
36. Ding, J.H.; Zhao, H.R.; Yu, H.B. High-yield synthesis of extremely high concentrated and few-layered boron nitride nanosheet dispersions. *2D Mater.* **2018**, *5*, 045015. [[CrossRef](#)]
37. Sainsbury, T.; O'Neill, A.; Passarelli, M.K.; Seraffon, M.; Gohil, D.; Gnaniyah, S.; Spencer, S.J.; Rae, A.; Coleman, J.N. Dibromocarbene functionalization of boron nitride nanosheets: Toward band gap manipulation and nanocomposite applications. *Chem. Mater.* **2014**, *26*, 7039–7050. [[CrossRef](#)]
38. Tian, X.; Li, Y.; Chen, Z.; Li, Q.; Hou, L.; Wu, J.; Tang, Y.; Li, Y. Shear-assisted production of few-layer boron nitride nanosheets by supercritical CO₂ exfoliation and its use for thermally conductive epoxy composites. *Sci. Rep.* **2017**, *7*, 17794. [[CrossRef](#)]
39. Li, W.; Song, Z.; Zhong, J.; Qian, J.; Tan, Z.; Wu, X.; Chu, H.; Nie, W.; Ran, X. Multilayer-structured transparent MXene/PVDF film with excellent dielectric and energy storage performance. *J. Mater. Chem. C* **2019**, *7*, 10371–10378. [[CrossRef](#)]
40. Feng, Y.; Li, M.L.; Li, W.L.; Zhang, T.D.; Zhao, Y.; Fei, W.D. Polymer/metal multi-layers structured composites: A route to high dielectric constant and suppressed dielectric loss. *Appl. Phys. Lett.* **2018**, *112*, 022901. [[CrossRef](#)]
41. American Society for Testing and Materials. *Standard Test Method for Dielectric Breakdown Voltage and Dielectric Strength of Solid Electrical Insulating Materials at Commercial Power Frequencies*; ASTM: West Conshohocken, PA, USA, 2013.
42. Danikas, M.G.; Tanaka, T. Nanocomposites—a review of electrical treeing and breakdown. *IEEE Electr. Insul. Mag.* **2009**, *25*, 19–25. [[CrossRef](#)]
43. Wu, W.; Liu, X.; Qiang, Z.; Yang, J.; Liu, Y.; Huai, K.; Zhang, B.; Jin, S.; Xia, Y.; Fu, K.K.; et al. Inserting insulating barriers into conductive particle channels: A new paradigm for fabricating polymer composites with high dielectric permittivity and low dielectric loss. *Compos. Sci. Technol.* **2021**, *216*, 109070. [[CrossRef](#)]
44. Wu, W.; Zhao, W.; Sun, Q.; Yu, B.; Yin, X.; Cao, X.; Feng, Y.; Li, R.K.; Qu, J. Surface treatment of two dimensional MXene for poly (vinylidene fluoride) nanocomposites with tunable dielectric permittivity. *Compos. Comm.* **2021**, *23*, 100562. [[CrossRef](#)]
45. Wang, L.; Luo, H.; Zhou, X.; Yuan, X.; Zhou, K.; Zhang, D. Sandwich-structured all-organic composites with high breakdown strength and high dielectric constant for film capacitor. *Compos. Part A Appl. Sci. Manuf.* **2019**, *117*, 369–376. [[CrossRef](#)]
46. Yu, S.; Zhang, J.; Zhu, X.; Yin, Y.; Xue, J.; Xia, F.; Li, Y.; Xue, Q. Plate-barrier architecture of rGO-TiO₂ derived from MXene for constructing well-aligned polymer nanocomposites with excellent dielectric performance. *Compos. Sci. Technol.* **2022**, *218*, 109191. [[CrossRef](#)]
47. Wang, B.; Yin, X.; Peng, D.; Zhang, Y.; Wu, W.; Gu, X.; Na, B.; Lv, R.; Liu, H. Highly thermally conductive PVDF-based ternary dielectric composites via engineering hybrid filler networks. *Compos. Part B Eng.* **2020**, *191*, 107978. [[CrossRef](#)]
48. Gu, J.; Lv, Z.; Wu, Y.; Guo, Y.; Tian, L.; Qiu, H.; Li, W.; Zhang, Q. Dielectric thermally conductive boron nitride/polyimide composites with outstanding thermal stabilities via in-situ polymerization-electrospinning-hot press method. *Compos. Part A Appl. Sci. Manuf.* **2017**, *94*, 209–216. [[CrossRef](#)]
49. Wu, K.; Lei, C.; Yang, W.; Chai, S.; Chen, F.; Fu, Q. Surface modification of boron nitride by reduced graphene oxide for preparation of dielectric material with enhanced dielectric constant and well-suppressed dielectric loss. *Compos. Sci. Technol.* **2016**, *134*, 191–200. [[CrossRef](#)]
50. Lin, B.; Li, Z.T.; Yang, Y.; Li, Y.; Lin, J.C.; Zheng, X.M.; He, F.A.; Lam, K.H. Enhanced dielectric permittivity in surface-modified graphene/PVDF composites prepared by an electrospinning-hot pressing method. *Compos. Sci. Technol.* **2019**, *172*, 58–65. [[CrossRef](#)]
51. Yang, C.; Hao, S.J.; Dai, S.L.; Zhang, X.Y. Nanocomposites of poly (vinylidene fluoride)-Controllable hydroxylated/carboxylated graphene with enhanced dielectric performance for large energy density capacitor. *Carbon* **2017**, *117*, 301–312. [[CrossRef](#)]
52. Li, C.Q.; Zha, J.W.; Long, H.Q.; Wang, S.J.; Zhang, D.L.; Dang, Z.M. Mechanical and dielectric properties of graphene incorporated polypropylene nanocomposites using polypropylene-graft-maleic anhydride as a compatibilizer. *Compos. Sci. Technol.* **2017**, *153*, 111–118. [[CrossRef](#)]
53. Hu, D.; Jiang, M.; Hou, Y.; Zhang, J.; Fang, D.; Liu, L.; Huang, J.; Li, H.; Xiong, C. Dielectric loss suppression of silver/poly (vinylidene fluoride) composite films with polydopamine. *J. Macromol. Sci. Part B Phys.* **2018**, *57*, 255–265. [[CrossRef](#)]
54. Hu, B.; Guo, H.; Wang, Q.; Zhang, W.; Song, S.; Li, X.; Li, Y.; Li, B. Enhanced thermal conductivity by constructing 3D-networks in poly (vinylidene fluoride) composites via positively charged hexagonal boron nitride and silica coated carbon nanotubes. *Compos. Part A Appl. Sci. Manuf.* **2020**, *137*, 106038. [[CrossRef](#)]

55. Wu, C.; Huang, X.; Wu, X.; Xie, L.; Yang, K.; Jiang, P. Graphene oxide-encapsulated carbon nanotube hybrids for high dielectric performance nanocomposites with enhanced energy storage density. *Nanoscale* **2013**, *5*, 3847–3855. [[CrossRef](#)]
56. Fang, X.; Liu, X.; Cui, Z.K.; Qian, J.; Pan, J.; Li, X.; Zhuang, Q. Preparation and properties of thermostable well-functionalized graphene oxide/polyimide composite films with high dielectric constant, low dielectric loss and high strength via in situ polymerization. *J. Mater. Chem. A* **2015**, *3*, 10005–10012. [[CrossRef](#)]
57. Luo, B.; Wang, X.; Wang, Y.; Li, L. Fabrication, characterization, properties and theoretical analysis of ceramic/PVDF composite flexible films with high dielectric constant and low dielectric loss. *J. Mater. Chem. A* **2014**, *2*, 510–519. [[CrossRef](#)]
58. Li, P.; Shen, H.; Qian, Z.; Yang, X.; Zhao, N.; Zhu, C.; Xu, J. Facile fabrication of flexible layered GO/BNNS composite films with high thermal conductivity. *J. Mater. Sci.* **2018**, *53*, 4189–4198. [[CrossRef](#)]
59. Chen, J.; Huang, X.; Sun, B.; Jiang, P. Highly thermally conductive yet electrically insulating polymer/boron nitride nanosheets nanocomposite films for improved thermal management capability. *ACS Nano* **2019**, *13*, 337–345. [[CrossRef](#)]
60. Chen, J.; Wei, H.; Bao, H.; Jiang, P.; Huang, X. Millefeuille-inspired thermally conductive polymer nanocomposites with overlapping BN nanosheets for thermal management applications. *ACS Appl. Mater. Interf.* **2019**, *11*, 31402–31410. [[CrossRef](#)]